processes

MDPI

Article

Nano-Hydroxyapatite Modified Tobacco Stalk-Based Biochar for Immobilizing Cd(II): Interfacial Adsorption Behavior and Mechanisms

Tianfu Li, Xiaofei Li *, Chaoran Shen, Dian Chen, Fuhua Li, Weicheng Xu, Xiaolian Wu and Yanping Bao

School of Environmental and Chemical Engineering, Foshan University, Foshan 528000, China
* Correspondence: xfli1103@fosu.edu.cn

Abstract: Biochar, an eco-friendly, porous carbon-rich material, is widely studied for immobilizing heavy metals in contaminated environments. This study prepared tobacco stalks, a typical agricultural waste, into biochar (TSB) modified by hydroxyapatite (HAP) at co-pyrolysis temperatures of 350 °C and 550 °C to explore its Cd(II) adsorption behavior and relevant mechanisms. XRD, SEM–EDS, FTIR, and BET analyses revealed that HAP successfully incorporated onto TSB, enriching the surface oxygen-containing functional groups (P–O and carboxyl), and contributing to the enhancement of the specific surface area from 2.52 (TSB350) and 3.63 m^2/g (TSB550) to 14.07 (HAP–TSB350) and 18.36 m^2/g (HAP–TSB550). The kinetics of Cd(II) adsorption onto TSB and HAP–TSB is well described by the pseudo-second-order model. Isotherm results revealed that the maximum adsorption capacities of Cd(II) on HAP–TSB350 and HAP–TSB550 were approximately 13.17 and 14.50 mg/g, 2.67 and 9.24 times those of TSB350 and TSB550, respectively. The Cd(II) adsorption amounts on TSBs and HAP–TSBs increased significantly with increasing pH, especially in HAP–TSB550. Ionic strength effects and XPS analysis showed that Cd(II) adsorption onto HAP–TSBs occurred mainly via electrostatic interaction, cation exchange with Ca^{2+}, complexation with P–O and –COOH, and surface precipitation. These findings will provide a modification strategy for the reutilization of tobacco agricultural waste in the remediation of heavy metal contaminated areas.

Keywords: tobacco stalk-based biochar; hydroxyapatite; cadmium; adsorption behavior; mechanisms

Citation: Li, T.; Li, X.; Shen, C.; Chen, D.; Li, F.; Xu, W.; Wu, X.; Bao, Y. Nano-Hydroxyapatite Modified Tobacco Stalk-Based Biochar for Immobilizing Cd(II): Interfacial Adsorption Behavior and Mechanisms. *Processes* **2024**, *12*, 1924. https://doi.org/10.3390/pr12091924

Academic Editor: Anna Wołowicz

Received: 13 August 2024
Revised: 3 September 2024
Accepted: 5 September 2024
Published: 7 September 2024

1. Introduction

As industries and agriculture progress rapidly, anthropogenic activities such as intensive mining, extensive industrial waste emissions, and the liberal application of agrochemicals frequently occur [1]. Poor management practices associated with these activities can inadvertently release heavy metals into the environment, particularly into aquatic and soil systems, thereby aggravating the serious problem of heavy metal pollution [2,3]. Cadmium (Cd), in particular, is acknowledged internationally for its high toxicity among heavy metals. It exhibits extreme environmental mobility and is frequently found in concentrations exceeding the standard limit, presenting a substantial threat to human health by causing kidney damage, bone demineralization, and increasing the risk of cancer [4,5]. Therefore, the control and remediation of Cd contamination has attracted widespread attention.

Biochar, which is a carbon-enriched material obtained from the pyrolysis of biomass under oxygen-restricted conditions, is characterized by its high structural stability, substantial specific surface area, elevated cation exchange capacity, and a plethora of oxygen-containing functional groups [6,7]. These properties collectively confer upon biochar a significant adsorptive capacity for heavy metals, positioning it as a viable and effective agent for the amelioration of heavy metal pollution in soils and aquatic environments [8,9]. The sources of biomass for the production of biochar are diverse, including crop residues (such as corn, rice, wheat, and tobacco stalks), garden waste (such as trimmings and fallen leaves), animal manure, and plant residues [10]. China has the largest tobacco cultivation

area in the world, spanning over 1.6 million hectares annually and generating an impressive three to five million tons of tobacco stalk waste [11,12]. This tobacco stalk waste, which poses a risk for the dissemination of diseases and insect pests, is precluded from use for direct soil amendment, and thereby classified as a hazardous agricultural byproduct [13]. Current disposal methods—predominantly, leaving the waste in the fields or incinerating it—are inefficient and contribute to environmental pollution and resource wastage [14]. Consequently, the pyrolysis of tobacco stalks into biochar offers an efficacious strategy not only for the valorization of agricultural residues but also for the remediation of heavy metal pollution, thereby enhancing the sustainable use of agricultural waste.

Currently, the adsorption effect of biochar alone is not ideal, and its application is still limited by its limited surface functional groups and specific surface area [15]. Therefore, the modification or functional regulation of biochar has become a research direction to stimulate the structural advantages and promote the large-scale application of biochar [16]. Modification methods of biochar can be divided into physical methods (ball milling, steaming, microwaving, etc.) [17–19], chemical methods (acid, alkali treatment, element doping, and mineral loading, etc.) [20–23], and biological methods (microbial colonization, anaerobic digestion, etc.) [24,25]. Among the various approaches, the application of cost-effective, high-performance minerals onto biochar is distinguished by its simplicity, affordability, and superior adsorptive properties, typically outperforming other biochar modifications in treatment efficacy [26].

Hydroxyapatite (HAP) is a favored adsorbent for its environmentally benign attributes, including non-toxicity, affordability, and minimal water solubility [27]. It has been extensively documented for its robust heavy metal adsorption capacity, which is ascribed to mechanisms such as ion exchange, surface complex formation, and dissolution–precipitation [26,28]. However, the high surface energy of HAP can result in aggregation, thereby potentially reducing its adsorptive efficiency [29]. Consequently, the integration of hydroxyapatite onto biochar to fabricate enhanced adsorbents has emerged as a focal point of research interest [26–28,30]. For example, Wang et al. (2018) found that HAP-modified rice straw-derived biochar exhibited more efficient adsorption for Pb(II), Cu(II), and Zn(II) compared to the raw biochar and HAP [29]. Chen et al. (2021) observed that HAP formed on sludge-based biochar showed excellent adsorption capacity for Cu(II) and Cd(II), using interfacial processes including ion exchange, surface complexion, and Cd-π or Cu-π surface binding [26]. Luo et al. (2022) also found that when HAP and biomass (wheat straw and dairy cow manure) were mixed and underwent co-pyrolysis under an N_2 atmosphere, they showed more Pb/Cd immobilization compared with the pristine biochar [27]. Although studies report similar results more and more, the type of biomass and the temperature and method of pyrolysis into biochar will also produce obvious differences in the physical and chemical properties and adsorption performance [16]. At present, research on the interfacial adsorption behavior of Cd(II) and its related mechanism in tobacco stalk-derived biochar (TSB) with HAP modification (HAP–TSB) is still lacking. Elucidating the role of HAP–TSB in modulating the mobility and bioavailability of heavy metals is crucial for devising strategies aimed at remediating specific kinds of environmental contamination and enhancing soil or water quality, thereby facilitating ecological restoration.

In our investigation, we selected tobacco stalks as the feedstock to synthesize a novel carbon-based composite material through co-pyrolysis at two different temperatures with hydroxyapatite. The microstructure and surface physicochemical properties of the synthesized materials were measured by employing scanning electron microscopy–energy dispersive spectroscopy (SEM–EDS), X-ray diffraction (XRD), Fourier transform infrared spectroscopy (FTIR), etc. Subsequent batch adsorption experiments were meticulously designed to explore the adsorption performance and behavior of Cd(II) on the TSBs and HAP–TSBs, encompassing studies on adsorption isotherms, kinetics, the influence of pH, and ionic strength. On this basis, X-ray photoelectron spectroscopy (XPS) was then employed to further reveal the interfacial interaction mechanisms of Cd(II) on the TSBs and HAP–TSBs surfaces. This study seeks to provide theoretical foundations and actionable

strategies to facilitate the full resource utilization of tobacco stalk waste, specifically targeting the remediation of cadmium pollution in both water and soil environments.

2. Materials and Methods

2.1. Experimental Materials

Tobacco stalk waste was collected from Guizhou Province, China, and subjected to rigorous cleaning using deionized water to eliminate residual soil and dust. Next, the biomass was dried in an oven at a temperature of 60 °C, crushed, and then stored for use in subsequent experiments and measurements. Hydroxyapatite powder (≥97% purity) and cadmium chloride (≥99% purity) were procured from Macklin (Shanghai Macklin Biochemical Co., Ltd., Shanghai, China). In addition, 1 M HCl and 1 M NaOH were employed to regulate the pH of the reaction system, while HNO_3 (5 wt%) was applied for the acidification of solution samples.

2.2. Tobacco Stalk-Derived Biochar and Its Modified Materials Preparation

Preparation of the tobacco stalk-derived biochar (TSB): The pretreated tobacco stalks were enclosed in aluminum foil and positioned inside a tubular furnace under a continuous nitrogen flow of 200 mL/min. The furnace temperature was ramped up to 350 °C and 550 °C at a heating rate of 10 °C /min, respectively, and then sustained for 2 h. After natural cooling, the TSB was pulverized, passed through a 100 mesh sieve, and stored in sealed bags under vacuum conditions for preservation. The two samples were labeled as TSB350 and TSB550, respectively.

Preparation of the hydroxyapatite modified biochar (HAP–TSB): TSB and HAP were homogeneously mixed in an aqueous solution at a weight ratio of 5:1 (*w*:*w*), after which the mixture was dried in an oven at a temperature of 60 °C until the moisture content was reduced to nearly 0% [27]. This specific ratio was chosen based on a review of previous studies and literature [31], balancing considerations for effectiveness and cost-efficiency. Subsequently, the mixture was transferred into a tubular furnace with a nitrogen atmosphere for pyrolysis. The pyrolysis conditions and subsequent treatment of the obtained composite were prepared through the established procedures for tobacco stalk biomass (TSB). The resulting functionalized biochar samples, derived from pyrolysis at specific temperatures, were designated as HAP–TSB350 and HAP–TSB550, respectively.

2.3. Batch Adsorption Experiment

To assess the adsorption performance of the prepared adsorbents for Cd(II) ions, a series of parameters were systematically investigated, including the initial concentration of Cd(II), contact time, pH, and ionic strength. For the adsorption isotherm experiments, 40 mg of each biochar and its modified samples were weighed and introduced into separate 30 mL glass bottles. Then 20 mL aliquots of Cd(II) solutions with various initial concentrations from 15 to 80 mg/L were added into their respective bottles. The adsorption process was carried out at 25 °C with continuous agitation at a rate of 180 r/min for 24 h. Throughout the experiment, the pH of the solutions were meticulously adjusted to a target value of 5.0 using 1 M HCl and NaOH solutions. After the reaction was completed, the supernatant was separated by filtration using a 0.45 μm polyether sulfone membrane filter. The filtered liquid was then acidified with HNO_3 (5 wt%), and the Cd(II) contents in the filtrate were measured with an atomic absorption spectrometer (AAS, model AA-6880, Shimadzu, Japan).

To ascertain the adsorption time effects, 400 mg of TSB and its modified samples were individually introduced into 200 mL of Cd(II) solution at 20 mg/L, with the pH adjusted to 5.0. The samples were then stirred using a magnetic stirrer set at 180 rpm to ensure thorough mixing of the solid–liquid system. At each pre-specified time point (2, 5, 10, 20, 30, 60, 120, 360, 480, and 720 min), 2 mL of the supernatant was extracted and subsequently passed through a 0.45 μm polyether sulfone membrane, and the Cd(II) concentration was then measured according to the above-mentioned methods.

To explore the influence of pH on the adsorption behavior of Cd(II) onto TSBs and HAP–TSBs, the solution pH was systematically adjusted to 2.5, 3.0, 3.5, 4.0, 5.0, and 6.0, and maintained using 1 M HCl and NaOH throughout the reaction. Ionic strength, including 0.01, 0.1, and 0.5 M NaCl, was selected in this study to elucidate the possible interfacial adsorption pathway of Cd(II). Once the reaction reached equilibrium, the mixture was filtered by employing a 0.45 μm polyether sulfone filter membrane, after which the Cd(II) concentration was then measured. To ensure the results were reliable, each experimental condition was replicated three times, and the data analysis was based on the calculated mean of these replicates.

2.4. Analytical Methods

The sorption capacity (Q_e, mg/g) was derived from the calculation that incorporated the initial concentration (C_0, mg/L) and the equilibrium concentration (C_e, mg/L) of the ions. Additionally, the adsorbent dosage (m/V, g/L) within the adsorption system was considered. The calculation was based on the following equation:

$$Qe = \frac{(C_0 - C_e) \times \mathrm{V}}{m} \quad (1)$$

To evaluate the adsorption capacity of the TSBs and HAP–TSBs, the experimental adsorption isotherm results were analyzed employing the Langmuir and Freundlich models [32,33]. Their corresponding equations are presented in Text S1 of the Supporting Information. Additionally, the kinetic data obtained from the adsorption time studies are analyzed employing pseudo-first-order and pseudo-second-order models to assess the nature of interfacial interactions and adsorption efficiency [30]. The models are shown in Text S2 of the Supporting Information. These equations facilitate the determination of kinetic parameters that describe the adsorption process.

2.5. Characterization of Experimental Samples

The crystalline phases of the synthesized TSBs and HAP–TSBs were characterized using an X-ray diffractometer (XRD, D8 Advance, Bruker, Germany) with Cu Kα radiation (λ = 1.5418 Å) conducted at 40 kV and 40 mA. The morphologies and microstructures of the TSBs and HAP–TSBs were examined with a scanning electron microscope (SEM, Carl Zeiss Microscopy, München, Germany) that was coupled with an energy dispersive spectrometer (EDS). The specific surface areas of the TSBs and HAP–TSBs were analyzed utilizing an AUTOSORB IQ Quantchrome analyzer (Quantchrome, Boynton Beach, FL, USA). The functional groups on the TSBs' and HAP–TSBs' surfaces were identified using Fourier transform infrared spectroscopy (FTIR, Perkin-Elmer, Shelton, CT, USA). The changes in surface chemical species, including C, O, and Cd elements, on the TSB and HAP–TSB surface after Cd(II) adsorption were ascertained using X-ray photoelectron spectroscopy with a ULVAC-PHI analyzer (XPS, ULVAC-PHI, Incorporated, Tokyo, Japan), which employed a monochromatic Al Kα X-ray (1486.6 eV).

3. Results and Discussions

3.1. Characterization of the Biochar with Modification

The crystal phase components of TSB and HAP–TSB were investigated by examining their XRD patterns. As depicted in Figure 1a,b, the diffraction peaks corresponding to the Whewellite phase are observable in TSB350. However, these peaks are nearly absent in TSB550, with additional peaks corresponding to calcite becoming apparent. This suggests that an increase in hydrolysis temperature facilitated a phase transformation. Furthermore, the XRD patterns of both HAP–TSB350 and HAP–TSB550 exhibit distinct diffraction peaks that can be attributed to the crystalline structure of hydroxyapatite (HAP). This observation confirmed that HAP had been successfully incorporated onto the surfaces of the TSB.

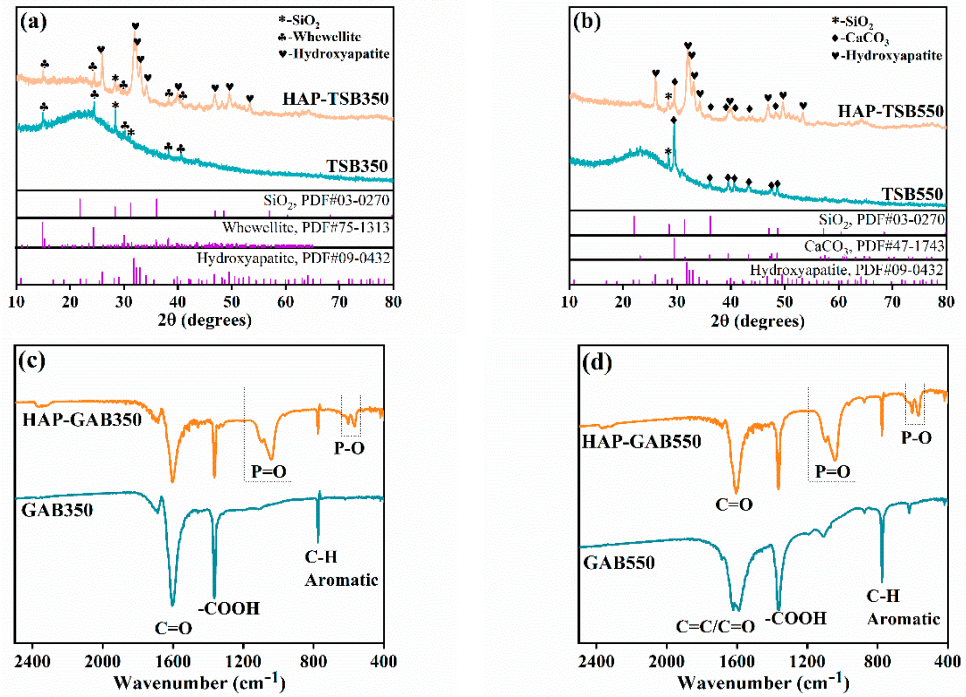

Figure 1. XRD patterns of HAP–TSB350 (**a**) and HAP–TSB550 (**b**), and their corresponding FTIR analyses (**c**,**d**).

The surface functional groups of TSB and HAP–TSB were characterized employing Fourier transform infrared (FTIR) spectroscopy. As shown in Figure 1c,d, the FTIR results of both HAP–TSB350 and HAP–TSB550 reveal characteristic stretching vibration absorption bands at 963, 1042, and 1094 cm^{-1}, and bending vibration absorption bands at 568 and 609 cm^{-1}, which correspond to P–O bonds. These findings indicate that the composite materials were enriched with phosphorus-containing structures, as referenced in the literature [28,34]. For TSB350, a prominent peak is observed at 1604 cm^{-1}, which can be attributed to the vibration of C=O groups [35]. In contrast, TSB550 exhibits a split peak with distinct overlapping bands at 1634 and 1591 cm^{-1}, corresponding to aromatic C=C stretches and the symmetric stretching of carboxylate groups [36]. This observation suggests that elevated temperatures may degrade the oxygen-containing active groups, thereby promoting the formation of aromatic structures [37]. Interestingly, the spectral shape in the corresponding wavenumber region for HAP–TSB550 showed almost no change compared to TSB550. This suggests that the incorporation of HAP helped to preserve the oxygen-containing active groups and reduced the relative proportion of aromatic structures. Additionally, the bands at 1370 and 782 cm^{-1} are indicative of the asymmetric stretching vibrations of the carboxylate group ($–COO^-$) and the aromatic C–H bonds, respectively [35,36,38,39]. Furthermore, the relative intensity of the aromatic C–H peak in TSB550 is considerably higher than that in TSB350, which implies an enhancement in aromaticity with increased hydrolysis temperature [40]. The FTIR analysis demonstrated that TSBs modified with HAP possess carboxylic groups and newly formed P–O functional groups, which might be responsible for Cd(II) adsorption, and exhibit better performance than raw TSBs.

The SEM images revealed that the TSBs exhibited distinctly porous architecture. In contrast, the surface porosity was partially obscured by the presence of hydroxyapatite crystals following the HAP modification (Figure 2a–d). Moreover, the mapping image (Figure 2e–h) and EDS spectra (Figure 2i–l) revealed that the P content of the hydroxyapatite modified biochars HAP–TSB350 and HAP–TSB550 was 5% and 2.5%, respectively. These levels are markedly higher than the P content found in their unmodified counterparts TSB350 (1.2%) and TSB550 (0.2%), indicating the successful integration of a considerable amount of hydroxyapatite (HAP) onto the biochar structure. The specific surface areas of

TSB350 and TSB550 were measured to be 2.52 m^2/g and 3.63 m^2/g, respectively, suggesting that higher hydrolysis temperatures can yield biochar with increased specific surface areas [37]. Upon modification with hydroxyapatite (HAP), the specific surface areas of HAP–TSB350 and HAP–TSB550 notably increased to 14.07 m^2/g and 18.36 m^2/g, respectively, which might be ascribed to the dispersion of HAP by TSB surfaces [41]. These enhancements are considerably higher than those in the raw TSBs, implying that the HAP–TSBs possess an increased availability of surface sites for toxic ion adsorption.

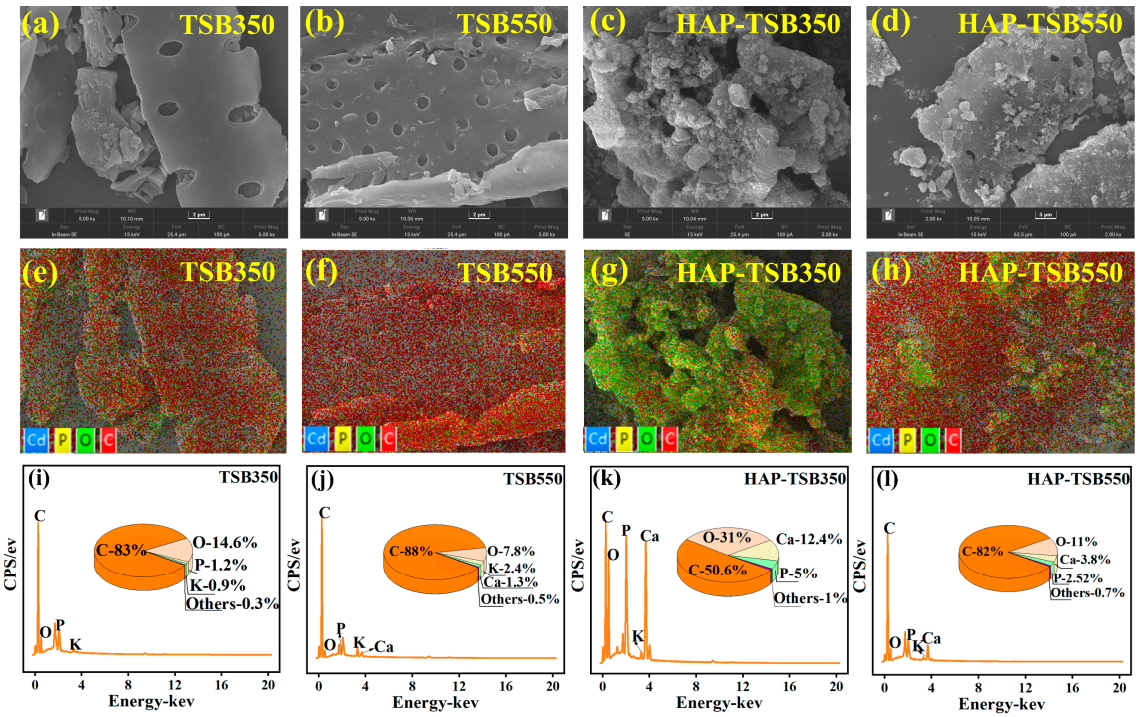

Figure 2. SEM images of TSB350 (**a**), TSB550 (**b**), HAP–TSB350 (**c**), and HAP–TSB550 (**d**) and their elemental mapping (**e**–**h**) and EDS results (**i**–**l**).

3.2. Adsorption Isotherm

Adsorption isotherm studies are pivotal for quantifying the extent to which Cd(II) ions are adsorbed onto the solid phase interfaces of adsorbents, thereby providing insights into their mobility and retention characteristics. Figure 3 presents the sorption isotherms for Cd(II) onto the TSBs and HAP–TSBs at varying concentrations. The isotherms for Cd(II) sorption on these materials exhibit a characteristic L-shaped curve with a plateau, which is indicative of possible homogeneous or heterogeneous precipitation events occurring alongside the interfacial interaction process [17]. Furthermore, the adsorption–isotherm curve for Cd(II) on TSB350 is observed to be elevated relative to that of TSB550 (Figure 3a). Additionally, both HAP–TSB350 and HAP–TSB550 demonstrate significantly enhanced sorption capacities when compared to their non-modified TSB counterparts prepared at equivalent pyrolysis temperatures (Figure 3b).

To comprehensively assess the maximum adsorption capacity and to deduce the adsorption mechanisms, the equilibrium data were interpreted through Langmuir and Freundlich models. The graphical representations of the Langmuir and Freundlich isotherm fits are displayed in Figure 3a and 3b, respectively, with the corresponding parameters of the isotherms listed in Table 1. For TSB350 and TSB550, the experimental data were found to be well-fitted with both the Langmuir and Freundlich models, as evidenced by the determined R-squared (R^2) values. Specifically, TSB350 was more suitably fitted by the Langmuir model, implying the existence of a monolayer adsorption process [28,41,42]. Conversely, TSB550 was better represented by the Freundlich model, which implies a favorable scenario for multilayer adsorption and chemical adsorption [34,43].

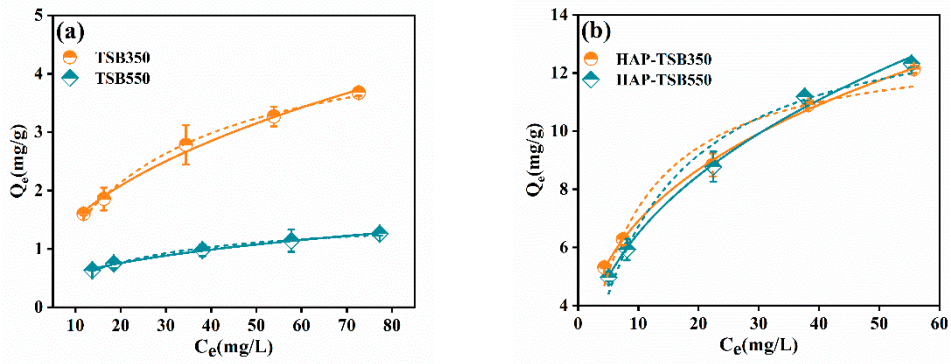

Figure 3. The sorption isotherms of Cd(II) on the TSBs (**a**) and HAP–TSBs (**b**) at a temperature of 298 K. The dashed lines denote Langmuir model fits, while the solid lines correspond to Freundlich model fits.

Table 1. Equilibrium adsorption isotherm fitting parameters.

Parameters	TSB350	TSB550	HAP–TSB350	HAP–TSB550
Langmuir				
Q_{max}	4.92	1.57	13.17	14.50
K_L	0.038	0.048	0.127	0.086
R^2	0.995	0.988	0.939	0.966
Freundlich				
1/n	0.45	0.38	0.33	0.39
K_F	0.54	0.24	3.23	2.66
R^2	0.991	0.995	0.998	0.993

Meanwhile, the experimental data for Cd(II) adsorption onto HAP–TSBs were found to be exclusively well-fitted by the Freundlich model. This phenomenon might be ascribed to the incorporation of HAP, which introduced additional active adsorption sites, resulting in complex interactions between Cd(II) ions and the modified biochar surfaces during the adsorption process. Conclusively, the Freundlich model is deemed appropriate for representing the adsorptive behavior of Cd(II) on the surfaces of TSBs and HAP–TSBs. From this perspective, the n values are found to be less than 1, signifying that the adsorption initially occurs at high energy sites, which are occupied before the subsequent uptake at lower energy sites on the heterogeneous surfaces [44,45]. The Freundlich constant K_F for TSB350 was 0.54, which was higher than the value of 0.24 observed for TSB550, indicating that the lower pyrolysis temperature of TSB350 resulted in a higher availability of high-affinity adsorption sites for Cd(II) [37,46]. Moreover, the K_F constants for the HAP-modified biochars (HAP–TSB350 and HAP–TSB550) were 3.23 and 2.66, respectively, which are substantially higher than those for their corresponding unmodified biochars, suggesting that the incorporation of HAP onto the TSBs introduces additional P–O binding sites, exhibiting strong bonding to Cd(II) [46]. Nevertheless, our tobacco stalk-derived biochars show lower adsorption performance than the results documented by Zhou et al. [47] and Yu et al. [14]. This might be attributed to differences in pyrolysis procedures, including temperature, heating rate, pyrolysis time, and mixing states, affecting the molecular components and reactivity [30]. On the other hand, composites modified with hydroxyapatite display significantly enhanced efficiency. Overall, the substantial improvement in the adsorptive capacity of tobacco stalk-derived biochar offers strategies for advancing the resourceful utilization of waste byproducts.

3.3. Adsorption Kinetics

The kinetic data for Cd(II) sorption onto TSBs and HAP–TSBs are displayed in Figure 4. The interfacial interactions between Cd(II) and the surfaces of the TSBs and HAP–TSBs occurred rapidly in the initial stage, then the rate of interaction decelerated as the system

reached sorption equilibrium. The Cd(II) adsorption equilibrium for HAP–TSB350 and HAP–TSB550 was achieved in around 60 min, with corresponding adsorption capacities of 5.7 mg/g and 6.6 mg/g, respectively. In contrast, the equilibrium for TSB350 and TSB550 was reached more quickly—in approximately 30 min and 5 min, respectively—with lower adsorption capacities of 1.9 mg/g and 1.1 mg/g. Meanwhile, the adsorption capacities for the HAP–TSBs substantially exceeded those of the TSBs at equivalent time points, suggesting that the incorporation of HAP significantly enhanced the adsorption kinetics and overall capacity. The different responses in Cd(II) adsorption kinetic behavior between TSBs and HAP–TSBs can likely be attributed to variations in the distribution and concentration of adsorption sites, including the presence of HAP phases as well as oxygen-containing functional groups on the TSBs' surfaces [41].

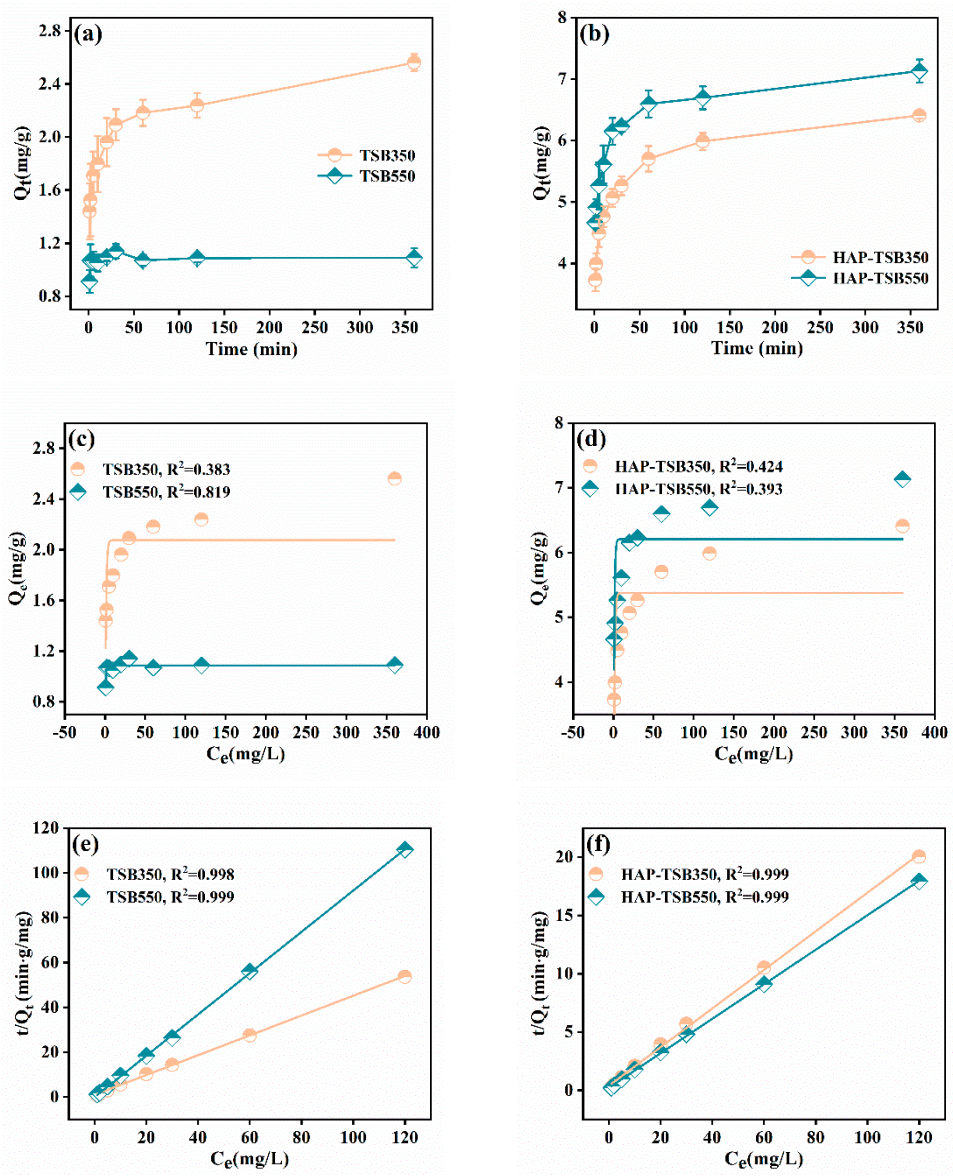

Figure 4. The kinetic plots for Cd(II) adsorption on TSBs' (**a**) and HAP–TSBs' (**b**) surfaces. The corresponding results fitted via the pseudo-first-order and pseudo-second-order model for TSBs (**c**,**e**) and HAP–TSBs (**d**,**f**).

The adsorption data were also subjected to kinetic modeling to shed light on the underlying sorption mechanisms. The pseudo-second-order model (Figure 4e–f) demonstrated a superior fit for the kinetic data compared to the pseudo-first-order model (Figure 4c,d) according to the correlation coefficients (R^2) and the calculated equilibrium adsorption

amounts (Q_e) (Table 2). Generally, adherence to a pseudo-second-order model implies that the rate-limiting step in the adsorption process is likely a chemical sorption mechanism [17,26]. Consequently, the uptake of Cd(II) onto the adsorption sites of the TSBs and HAP–TSBs is predominantly governed by chemical interactions such as ion exchange, surface complexation, and/or precipitation. These chemical reactions are the primary drivers, rather than physical adsorption, in the sorption process [17]. Furthermore, the rate of Cd(II) adsorption onto the TSBs, particularly TSB550, was considerably higher than adsorption onto the HAP–TSBs. This increased rate is primarily due to a lower density of active surface sites on TSBs that are available for Cd(II) adsorption, which allows for a more rapid attainment of equilibrium in the interfacial reaction. Conversely, the TSBs modified with HAP exhibited superior adsorption capacity compared to the unmodified TSBs even at the same time intervals. This enhanced performance is attributed to the abundance of functional groups present in these HAP–TSBs, which facilitate more extended interfacial adsorption processes, thereby slowing the rate at which equilibrium is achieved.

Table 2. Kinetic parameters of Cd(II) adsorption onto the TSBs and HAP–TSBs.

	Pseudo-First-Order Model			**Pseudo-Second-Order Model**		
	Q_e	**K_1**	**R^2**	**Q_e**	**K_2**	**R^2**
TSB350	2.08	0.89	0.383	2.26	0.24	0.997
TSB550	1.09	1.85	0.819	1.09	3.94	0.999
HAP–TSB350	5.37	0.91	0.424	6.04	0.07	0.999
HAP–TSB550	1.13	6.21	0.393	6.76	0.11	0.999

3.4. Effects of pH and Ionic Strength

pH is a critical environmental parameter when assessing the utility of a material, as it significantly affects the surface charge distribution of the solid phase, its sorption capabilities, and Cd(II) speciation in aqueous solutions [34]. As documented in previous studies [17], the prevailing species of Cd(II) in aqueous solutions at a pH of 2.5 to 6.0 are the positively charged hydrated ions. The non-occurrence of hydroxide precipitation under these conditions suggests that Cd(II) is attached to the surfaces of the TSBs and HAP–TSBs via direct interactions with the active adsorption sites.

The pH-dependent sorption curves of Cd(II) onto the TSBs and HAP–TSBs are depicted in Figure 5. It is evident that the sorption capacity for Cd(II) augmented with an increase in pH from 2.5 to 6.0. Moreover, the sorption capacities of the HAP–TSBs were significantly greater than those of the unmodified TSBs. Furthermore, at lower pH values, a higher concentration of H^+ or H_3O^+ ions was present, which can compete for and occupy active sites [48], and particularly affected the less oxygen-rich functional groups of TSB550, leading to a reduced adsorption capacity for Cd(II). However, the presence of hydroxyapatite (HAP) on the TSB surface introduced a plethora of adsorption sites characterized by P–O bonds and resulted in a decrease in surface charge [26,49]. This modification enhanced the TSBs' ability to adsorb Cd(II), even at lower pH levels, by providing additional binding sites. With the progression of pH elevation, the deprotonation of active groups on the TSBs and HAP–TSBs surfaces resulted in an increasingly negatively charged interface [49]. Consequently, this promoted a substantial electrostatic attraction to Cd(II) in the aqueous solutions. Broadly speaking, as the pH increased, the degree of deprotonation of the active groups diminished, enabling a greater availability of P–O and oxygen-containing adsorption sites [26]. This availability facilitated the easy occupation of the vacant orbitals of Cd atoms, which in turn significantly enhanced the formation of surface complexes [17]. Therefore, the adsorption of Cd(II) on the HAP–TSBs was significantly more effective than that on the TSBs, even at high pH values.

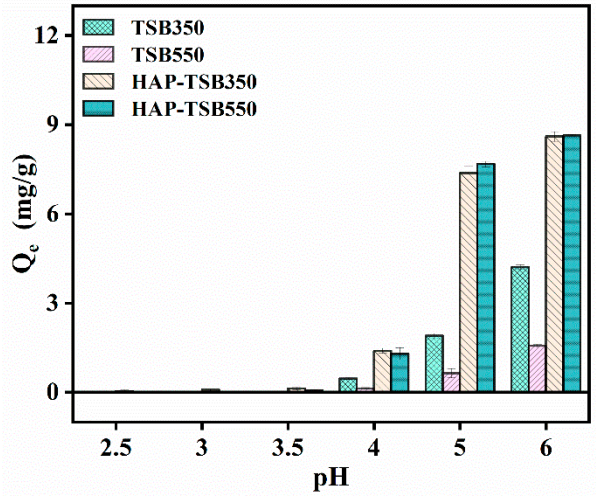

Figure 5. Effects of pH on Cd(II) adsorption onto TSB350, TSB550, HAP–TSB350, and HAP–TSB550 surfaces.

Frequently, observing the interfacial adsorption behavior across various ionic strengths provides insight into the mechanisms responsible for the adsorption of heavy metals by materials in an aqueous system [50]. Figure 6 illustrates the impact of ionic strength, varying from 0.01 to 0.5 mol/L, on the efficacy of the adsorbents. The results show that Cd(II) adsorption onto both the TSBs and HAP–TSBs declined with an increase in the initial NaCl concentration. The evident reliance of sorption on ionic strength suggests that cation exchange and/or outer-sphere complexation, facilitated by electrostatic interactions [51], were the predominant mechanisms responsible for the immobilization of Cd(II) on the surfaces of the TSBs and HAP–TSBs.

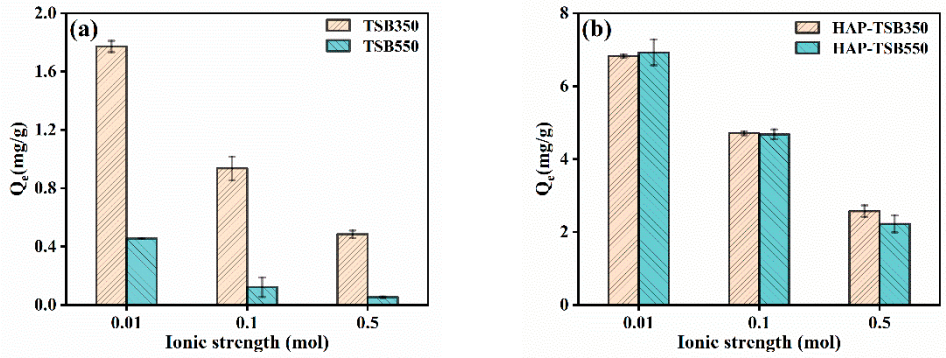

Figure 6. Effects of ionic strength on Cd(II) adsorption onto the TSBs' (**a**) and HAP–TSBs' (**b**) surfaces.

Specifically, the Cd(II) adsorption capacity of TSB350 dropped to 0.48 mg/g under a 0.5 M NaCl solution, a value that significantly exceeded the 0.05 mg/g observed for TSB550. This disparity suggests that TSB350, synthesized at a relatively low pyrolysis temperature, possesses more abundant oxygen-containing active groups that are available for chemically binding Cd(II), thus enhancing its adsorption capacity. Furthermore, the adsorption of Cd(II) on HAP–TSB350 and HAP–TSB550 was reduced to 2.56 and 2.22 mg/g under the condition of 0.5 M NaCl, respectively. Despite this reduction, these values are still significantly higher than the adsorption amounts of the unmodified TSBs. This sustained high adsorption capacity suggests that the HAP phases actively contribute to the interfacial adsorption process and promote the formation of Cd(II) inner-sphere surface complexes.

3.5. X-ray Photoelectron Spectroscopy Analysis

X-ray photoelectron spectroscopy (XPS) was employed to analyze the TSBs and HAP–TSBs before and after Cd(II) adsorption, providing detailed insights into the specific surface

chemical species alterations that occurred [34,50]. In contrast to the XPS survey spectra of the TSBs, the presence of characteristic P 2p and Ca 2p peaks in the spectra of the HAP–TSBs confirms the successful deposition of HAP onto the TSB surface (Figure 7a). Concurrently, the Cd 3d peaks detected in the XPS spectra of Cd–HAP–TSB350 and Cd–HAP–TSB550 are more pronounced than those observed in the Cd–TSBs. This suggests that the composite materials have a higher affinity for Cd(II) immobilization. Moreover, the relative intensity of the Ca 2p peak, normalized to that of the C 1s peak, indicated a reduction in the adsorption of Cd(II) onto the HAP–TSBs. This finding suggests that cation exchange is a contributing mechanism for the interaction of Cd(II) with the surfaces of HAP–TSBs [26].

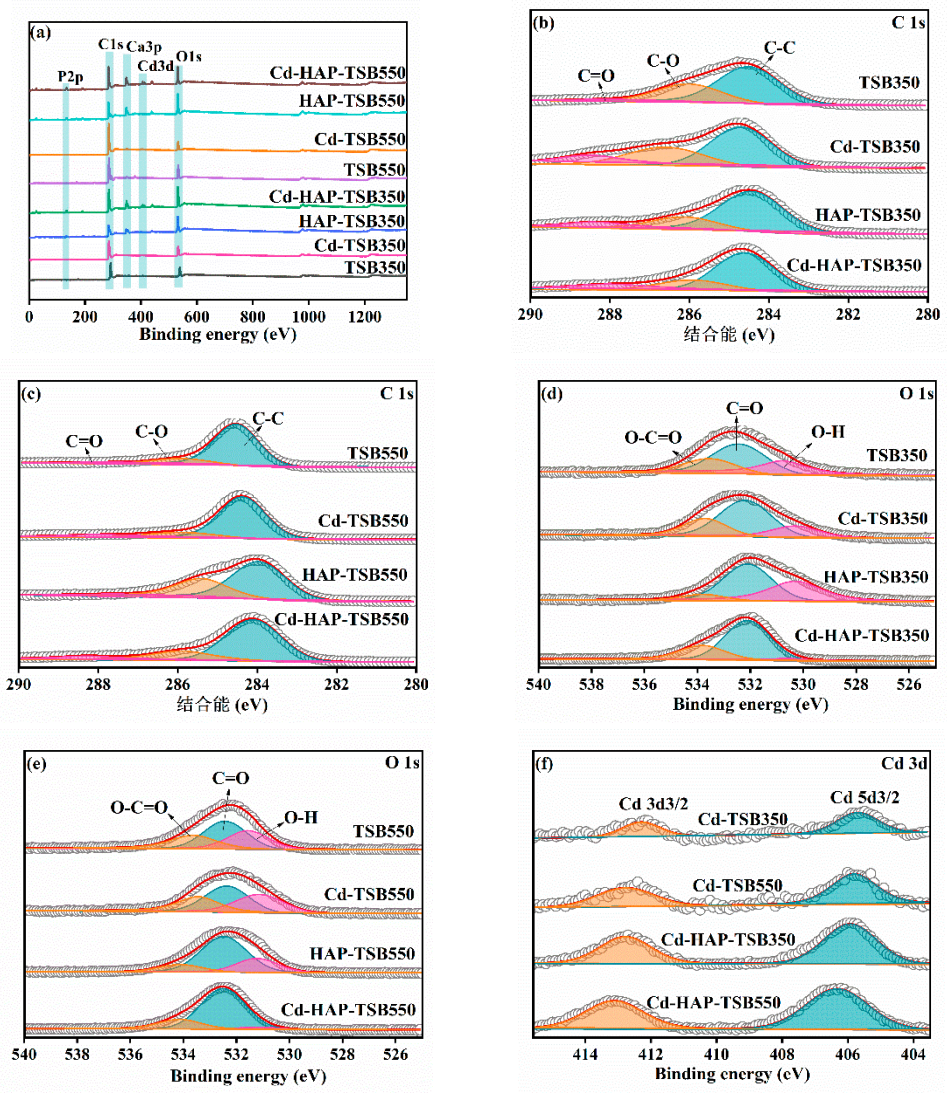

Figure 7. The spectra of the TSBs and HAP–TSBs before and after the adsorption of Cd(II): (**a**) survey spectra, (**b**,**c**) C 1s, (**d**,**e**) O 1s, and (**f**) Cd 3d.

The deconvoluted C 1s spectra are depicted in Figure 7b,c. A comparison of the C 1s spectra with TSB350, HAP–TSB350, TSB550, and HAP–TSB550 reveals that the relative ratio of the peaks corresponding to the C–O group at binding energies of 285.9 to 286.6 eV is notably reduced following Cd adsorption (Table 3), suggesting the formation of Cd-carboxyl complexes on the surfaces of the materials [52]. Simultaneously, there is a significant increase in the peak ratio of the C=O group within the binding energy range of 288.3 to 288.5 eV after Cd(II) adsorption, implying that carbonate precipitation may have occurred during the adsorption process [30].

Table 3. The deconvolution of C and O species for the TSBs', HAP–TSBs', Cd–TSBs', and Cd–HAP–TSBs' reaction systems and the corresponding peak area ratio.

	C Speciation Proportion (%)			O Speciation Proportion (%)		
	C–C	C–O	C=O	O–C=O	C=O	O–H
TSB350	65.59	31.57	2.84	21.18	47.28	31.54
Cd–TSB350	50.62	28.25	21.13	23.30	55.87	20.83
HAP–TSB350	68.84	19.33	11.83	8.49	49.55	41.96
Cd–HAP–TSB350	61.52	18.08	20.40	26.26	67.55	6.19
TSB550	85.06	10.96	3.98	27.17	42.60	30.23
Cd–TSB550	77.33	10.76	11.91	28.55	43.63	27.82
HAP–TSB550	63.83	33.02	3.15	12.18	64.93	22.89
Cd–HAP–TSB550	69.79	20.08	10.13	19.59	76.24	4.17

After the sorption of Cd(II), the O 1s XPS spectra of Cd–TSB350, Cd–HAP–TSB350, Cd–TSB550, and Cd–HAP–TSB550 exhibit an elevated peak ratio for the carbonate structures (O–C=O or CO_3^{2-}) (Figure 7d,e). Simultaneously, there is a pronounced reduction in the O–H peak. This suggests that, following sorption, carbonate-related products, including cadmium carbonates, are formed and active oxygen-containing groups on the sorbent surfaces are engaged in complexation with Cd(II) [26,53]. Notably, the O 1s spectra of Cd–HAP–TSBs exhibit a more pronounced alteration in the relative ratio of O–H to O–C=O peaks (Table 3), which might be ascribed to interfacial reactions involving the high oxygen-containing active sites of the HAP phase [30]. Furthermore, the Cd 3d XPS spectra revealed that the peaks corresponding to Cd 3d3/2 and Cd 5d3/2 shifted to higher binding energies on the HAP–TSBs. Additionally, there was a notable increase in the intensity of these peaks on the surface of the Cd–HAP–TSBs. These observations suggest that the HAP modification enhanced Cd(II) adsorption and led to the formation of more stable surface complexes.

4. Conclusions

In this investigation, the TSBs and HAP–TSBs produced through pyrolysis at different temperatures were systematically evaluated by analyzing their microstructures, elemental distribution, specific surface area, functional groups, adsorption performance for Cd(II), and underlying mechanisms governing interfacial interactions. The TSBs modified with HAP resulted in a notable expansion of their surface-specific area and an alteration in the composition of active sites, such as P–O and carboxyl groups. Among these synthesized materials, HAP–TSB550 exhibited superior and effective Cd(II) adsorption, which is primarily attributed to its large specific surface area in conjunction with the presence of incorporated HAP. The adsorption kinetics of Cd(II) onto the HAP–TSBs were found to conform closely to the pseudo-second-order model, whilst the isotherms were well described by the Freundlich model. The dominant mechanisms of Cd(II) adsorption onto the HAP–TSBs include cation exchange, surface inner-sphere complexation, surface precipitation, and outer-sphere complexation (electrostatic attraction), which are facilitated by the co-existence of abundant oxygen-containing and phosphate groups. Overall, the adsorption performance of Cd(II) on HAP–TSB350 is as efficient as on HAP–TSB550, demonstrating that modification with HAP at a low pyrolysis temperature is more economical and has greater applicability. The HAP–TSBs developed in this study provide insight into their adsorption mechanisms and present a feasible approach for the effective reutilization of tobacco stalk waste and the remediation of areas with low-level heavy metal pollution, enhancing overall environmental quality.

Supplementary Materials: The following supporting information can be downloaded at: https://www.mdpi.com/article/10.3390/pr12091924/s1, Text S1: Langmuir and Freundlich isotherm models; Text S2: Adsorption kinetic models.

Author Contributions: T.L.: Investigation, Data curation, Methodology, Writing—original draft; X.L.: Conceptualization, Funding acquisition, Supervision, Writing—review & editing; C.S.: Investigation, Visualization; D.C.: Investigation, software; F.L.: Formal analysis, Writing—review and editing; W.X.: Visualization, Writing—review and editing; X.W.: Software, Writing—review & editing; Y.B.: Validation, Writing—review and editing. All authors have read and agreed to the published version of the manuscript.

Funding: This work was supported by the National Natural Science Foundation of China (Nos. 42307278, 42207302); the Guangdong Basic and Applied Basic Research Foundation, China (Nos. 2022A1515110918, 2022A1515110444); and the National Key Research and Development Program of China (No. 2023YFD17-00802).

Data Availability Statement: All relevant data has been included in the article.

Conflicts of Interest: The authors declare no competing financial interests.

References

1. Oh, S.Y.; Yoon, M.K. Biochar for Treating Acid Mine Drainage. *Environ. Eng. Sci.* **2013**, *30*, 589–593. [CrossRef]
2. Xiang, M.T.; Li, Y.; Yang, J.Y.; Lei, K.G.; Li, Y.; Li, F.; Zheng, D.F.; Fang, X.Q.; Cao, Y. Heavy metal contamination risk assessment and correlation analysis of heavy metal contents in soil and crops. *Environ. Pollut.* **2021**, *278*, 116911. [CrossRef] [PubMed]
3. He, L.Z.; Xu, Y.; Zhang, M.E.; Gul, S.; Zhang, X.K.; Zhong, H.; Tang, Y.X.; Dong, D.B.; Xu, Y.; Liu, D.; et al. Effect of remediation technologies on soil fertility in heavy metal(loid)-contaminated soils: A critical review. *Crit. Rev. Environ. Sci. Technol.* **2024**, *54*, 1417–1435. [CrossRef]
4. Liu, T.; Yuan, X.M.; Luo, K.; Xie, C.; Zhou, L.Y. Molecular engineering of a new method for effective removal of cadmium from water. *Water. Res.* **2024**, *253*, 121326. [CrossRef]
5. Lange, K.; Viklander, M.; Blecken, G.T. Investigation of intra-event variations of total, dissolved and truly dissolved metal concentrations in highway runoff and a gross pollutant trap—Bioretention stormwater treatment train. *Water. Res.* **2022**, *216*, 118284. [CrossRef] [PubMed]
6. Gao, Y.R.; Chen, H.B.; Fang, Z.; Niazi, N.K.; Adusei-Fosu, K.; Li, J.H.; Yang, X.; Liu, Z.Z.; Bolan, N.S.; Gao, B.; et al. Coupled sorptive and oxidative antimony(III) removal by iron-modified biochar: Mechanisms of electron-donating capacity and reactive Fe species. *Environ. Pollut.* **2023**, *337*, 122637. [CrossRef]
7. Inyang, M.I.; Gao, B.; Yao, Y.; Xue, Y.W.; Zimmerman, A.; Mosa, A.; Pullammanappallil, P.; Ok, Y.S.; Cao, X.D. A review of biochar as a low-cost adsorbent for aqueous heavy metal removal. *Crit. Rev. Environ. Sci. Technol.* **2016**, *46*, 406–433. [CrossRef]
8. Tran, H.T.; Bolan, N.S.; Lin, C.; Binh, Q.A.; Nguyen, M.K.; Luu, T.A.; Le, V.G.; Pham, C.Q.; Hoang, H.G.; Vo, D.V.N. Succession of biochar addition for soil amendment and contaminants remediation during co-composting: A state of art review. *J. Environ. Manag.* **2023**, *342*, 118191. [CrossRef]
9. Biswal, B.K.; Balasubramanian, R. Use of biochar as a low-cost adsorbent for removal of heavy metals from water and wastewater: A review. *J. Environ. Chem. Eng.* **2023**, *11*, 110986. [CrossRef]
10. Fakayode, O.A.; Aboagarib, E.A.A.; Zhou, C.S.; Ma, H.L. Co-pyrolysis of lignocellulosic and macroalgae biomasses for the production of biochar—A review. *Bioresour. Technol.* **2020**, *297*, 122408. [CrossRef]
11. Yang, X.; Lu, K.; McGrouther, K.; Che, L.; Hu, G.; Wang, Q.; Liu, X.; Shen, L.; Huang, H.; Ye, Z.; et al. Bioavailability of Cd and Zn in soils treated with biochars derived from tobacco stalk and dead pigs. *J. Soils Sediments* **2017**, *17*, 751–762. [CrossRef]
12. Zhang, W.; Li, C.; Li, G.; Lin, Q.; Zhao, X.; He, Y.; Liu, Y.; Luo, Z. Biochar alters inorganic phosphorus fractions in tobacco-growing soil. *J. Soil Sci. Plant Nut.* **2021**, *21*, 1689–1699. [CrossRef]
13. Zheng, X.; Song, W.; Guan, E.; Wang, Y.; Hu, X.; Liang, H.; Dong, J. Response in physicochemical properties of tobacco-growing soils and N/P/K accumulation in tobacco plant to tobacco straw biochar. *J. Soil Sci. Plant Nutr.* **2020**, *20*, 293–305. [CrossRef]
14. Yu, X.N.; Zhou, H.J.; Ye, X.F.; Wang, H.L. From hazardous agriculture waste to hazardous metal scavenger: Tobacco stalk biochar-mediated sequestration of Cd leads to enhanced tobacco productivity. *J. Hazard. Mater.* **2021**, *413*, 125303. [CrossRef] [PubMed]
15. Awasthi, M.K. Engineered biochar: A multifunctional material for energy and environment. *Environ. Pollut.* **2022**, *298*, 118831. [CrossRef]
16. Chen, H.B.; Gao, Y.R.; Li, J.H.; Fang, Z.; Bolan, N.; Bhatnagar, A.; Gao, B.; Hou, D.Y.; Wang, S.S.; Song, H.; et al. Engineered biochar for environmental decontamination in aquatic and soil systems: A review. *Carbon Res.* **2022**, *1*, 4. [CrossRef]
17. Xiao, J.; Hu, R.; Chen, G.C. Micro-nano-engineered nitrogenous bone biochar developed with a ball-milling technique for high-efficiency removal of aquatic Cd(II), Cu(II) and Pb(II). *J. Hazard. Mater.* **2020**, *387*, 121980. [CrossRef]
18. Duan, W.Y.; Oleszczuk, P.; Pan, B.; Xing, B.S. Environmental behavior of engineered biochars and their aging processes in soil. *Biochar* **2019**, *1*, 339–351. [CrossRef]
19. Medeiros, D.; Nzediegwu, C.; Benally, C.; Messele, S.A.; Kwak, J.H.; Naeth, M.A.; Ok, Y.S.; Chang, S.X.; El-Din, M.G. Pristine and engineered biochar for the removal of contaminants co-existing in several types of industrial wastewaters: A critical review. *Sci. Total Environ.* **2022**, *809*, 151120. [CrossRef]

20. Li, M.P.; Dong, C.; Guo, C.X.; Yu, L.G. Magnetic activated biochar Fe_3O_4-MOS made from moringa seed shells for the adsorption of methylene blue. *Processes* **2022**, *10*, 2720. [CrossRef]
21. Lan, G.X.; Yan, X.X.; Deng, P.Y.; Li, T.Z.; Xia, Y.P.; Zhu, Z.H.; Wu, Y.; Fu, C.A. Preparation of iron salt-modified sludge biochar and its uptake behavior for phosphate. *Processes* **2022**, *10*, 2122. [CrossRef]
22. Chen, H.B.; Gao, Y.R.; Fang, Z.; Li, J.Y.; Pillai, S.C.; Song, H.C.; Sun, C.H.; Bolan, N.; Yang, X.; Vithanage, M.; et al. Investigating the electron-scale adsorption mechanisms using DFT calculations and experimental studies in self-assembly magnetic biochar gel incorporated with graphene nanosheets for enhanced Sb(III) removal. *Chem. Eng. J.* **2024**, *487*, 150740. [CrossRef]
23. Ban, S.E.; Lee, E.J.; Lim, D.J.; Kim, I.S.; Lee, J.W. Evaluation of sulfuric acid-pretreated biomass-derived biochar characteristics and its diazinon adsorption mechanism. *Bioresour. Technol.* **2022**, *348*, 126828. [CrossRef]
24. Bolan, S.; Hou, D.Y.; Wang, L.W.; Hale, L.; Egamberdieva, D.; Tammeorg, P.; Li, R.; Wang, B.; Xu, J.P.; Wang, T.; et al. The potential of biochar as a microbial carrier for agricultural and environmental applications. *Sci. Total Environ.* **2023**, *886*, 163968. [CrossRef] [PubMed]
25. Kumar, A.; Singh, E.; Mishra, R.; Kumar, S. Biochar as environmental armour and its diverse role towards protecting soil, water and air. *Sci. Total Environ.* **2022**, *806*, 150444. [CrossRef]
26. Chen, Y.N.; Li, M.L.; Li, Y.P.; Liu, Y.H.; Chen, Y.R.; Li, H.; Li, L.S.Z.; Xu, F.T.; Jiang, H.J.; Chen, L. Hydroxyapatite modified sludge-based biochar for the adsorption of Cu^{2+} and Cd^{2+}: Adsorption behavior and mechanisms. *Bioresour. Technol.* **2021**, *321*, 124413. [CrossRef]
27. Luo, Y.; Li, Z.P.; Xu, H.C.; Xu, X.Y.; Qiu, H.; Cao, X.D.; Zhao, L. Development of phosphorus composite biochar for simultaneous enhanced carbon sink and heavy metal immobilization in soil. *Sci. Total Environ.* **2022**, *831*, 154845. [CrossRef]
28. Zhu, Z.Q.; Yang, Y.H.; Fan, Y.M.; Zhang, L.H.; Tang, S.; Zhu, Y.N.; Zhou, X.B. Strontium-doped hydroxyapatite as an efficient adsorbent for Cd(II) removal from wastewater: Performance, kinetics, and mechanism. *Environ. Technol. Innov.* **2022**, *28*, 102575. [CrossRef]
29. Wang, Y.Y.; Liu, Y.X.; Lu, H.H.; Yang, R.Q.; Yang, S.M. Competitive adsorption of Pb(II), Cu(II), and Zn(II) ions onto hydroxyapatite-biochar nanocomposite in aqueous solutions. *J. Solid State Chem.* **2018**, *261*, 53–61. [CrossRef]
30. Sun, L.M.; Wu, J.S.; Wang, J.S.; Xu, M.; Zhou, W.Y.; Du, Y.C.; Li, Y.L.; Li, H.Y. Fabricating hydroxyapatite functionalized biochar composite using steel slag and Hami melon peel for Pb(II) and Cd(II) removal. *Colloids Surf. Physicochem. Eng. Aspects.* **2023**, *666*, 131310. [CrossRef]
31. Gao, R.; Fu, Q.; Hu, H.; Wang, Q.; Liu, Y.; Zhu, J. Highly-effective removal of Pb by co-pyrolysis biochar derived from rape straw and orthophosphate. *J. Hazard. Mater.* **2019**, *371*, 191–197. [CrossRef] [PubMed]
32. Langmuir, I. The Adsorption of gases on plane surfaces of glass, mica and platinum. *J. Am. Chem. Soc.* **1918**, *40*, 1361–1403. [CrossRef]
33. Freundlich, H.M.F. Über die adsorption in lösungen Z. *Phys. Chem.* **1906**, *57*, 385–470. [CrossRef]
34. Liao, J.; He, X.S.; Zhang, Y.; Zhang, L.; He, Z.B. The construction of magnetic hydroxyapatite-functionalized pig manure-derived biochar for the efficient uranium separation. *Chem. Eng. J.* **2023**, *457*, 141367. [CrossRef]
35. Li, J.Y.; Gao, Y.R.; Li, C.B.; Wang, F.L.; Chen, H.B.; Yang, X.; Jeyakumar, P.; Sarkar, B.; Luo, Z.B.; Bolan, N.; et al. Pristine and Fe-functionalized biochar for the simultaneous immobilization of arsenic and antimony in a contaminated mining soil. *J. Hazard. Mater.* **2024**, *469*, 133937. [CrossRef]
36. Qian, L.B.; Zhang, W.Y.; Yan, J.C.; Han, L.; Chen, Y.; Ouyang, D.; Chen, M.F. Nanoscale zero-valent iron supported by biochars produced at different temperatures: Synthesis mechanism and effect on Cr(VI) removal. *Environ. Pollut.* **2017**, *223*, 153–160. [CrossRef] [PubMed]
37. Das, S.K.; Ghosh, G.K.; Avasthe, R.K.; Sinha, K. Compositional heterogeneity of different biochar: Effect of pyrolysis temperature and feedstocks. *J. Environ. Manag.* **2021**, *278*, 111501. [CrossRef]
38. Yang, F.; Jiang, Y.T.; Dai, M.; Hou, X.T.; Peng, C.S. Active biochar-supported iron oxides for Cr(VI) removal from groundwater: Kinetics, stability and the key role of FeO in electron-transfer mechanism. *J. Hazard. Mater.* **2022**, *424*, 127542. [CrossRef]
39. Chia, C.H.; Gong, B.; Joseph, S.D.; Marjo, C.E.; Munroe, P.; Rich, A.M. Imaging of mineral-enriched biochar by FTIR, Raman and SEM-EDX. *Vib. Spectrosc.* **2012**, *62*, 248–257. [CrossRef]
40. Sun, Y.Q.; Xiong, X.N.; He, M.J.; Xu, Z.B.; Hou, D.Y.; Zhang, W.H.; Ok, Y.S.; Rinklebe, J.; Wang, L.L.; Tsang, D.C.W. Roles of biochar-derived dissolved organic matter in soil amendment and environmental remediation: A critical review. *Chem. Eng. J.* **2021**, *424*, 130387. [CrossRef]
41. Zhu, S.H.; Irshad, M.K.; Ibrahim, M.; Chen, Q.; Shang, J.Y.; Zhang, Q.R. The distinctive role of nano-hydroxyapatite modified biochar for alleviation of cadmium and arsenic toxicity in aqueous system. *J. Water Process. Eng.* **2022**, *49*, 103054. [CrossRef]
42. Li, X.F.; Guo, C.L.; Jin, X.H.; Yao, Q.; Liu, Q.Q.; Zhang, L.J.; Lu, G.N.; Reinfelder, J.R.; Huang, W.L.; Dang, Z. Molecular-scale study of Cr(vi) adsorption onto lepidocrocite facets by EXAFS, in situ ATR-FTIR, theoretical frequency calculations and DFT+ U techniques. *Environ. Sci. Nano* **2022**, *9*, 568–581. [CrossRef]
43. Zhang, Y.P.; Adi, V.S.K.; Huang, H.L.; Lin, H.P.; Huang, Z.H. Adsorption of metal ions with biochars derived from biomass wastes in a fixed column: Adsorption isotherm and process simulation. *J. Ind. Eng. Chem.* **2019**, *76*, 240–244. [CrossRef]
44. Li, Z.; Li, M.; Che, Q.; Li, Y.D.; Liu, X. Synergistic removal of tylosin/sulfamethoxazole and copper by nanohydroxyapatite modified biochar. *Bioresour. Technol.* **2019**, *294*, 122163. [CrossRef]

45. Liu, N.; Wang, M.X.; Liu, M.M.; Liu, F.; Weng, L.; Koopal, L.K.; Tan, W.F. Sorption of tetracycline on organo-montmorillonites. *J. Hazard. Mater.* **2012**, *225–226*, 28–35. [CrossRef]
46. Liu, C.W.; Ye, J.; Lin, Y.; Wu, J.; Price, G.W.; Burton, D.; Wang, Y.X. Removal of Cadmium (II) using water hyacinth (*Eichhornia crassipes*) biochar alginate beads in aqueous solutions. *Environ. Pollut.* **2020**, *264*, 114785. [CrossRef]
47. Zhou, Z.; Xu, Z.; Feng, Q.; Yao, D.; Yu, J.; Wang, D.; Lv, S.; Liu, Y.; Zhou, N.; Zhong, M.-E. Effect of pyrolysis condition on the adsorption mechanism of lead, cadmium and copper on tobacco stem biochar. *J. Clean. Prod.* **2018**, *187*, 996–1005. [CrossRef]
48. Li, Z.W.; Niu, R.Y.; Yu, J.H.; Yu, L.Y.; Cao, D. Removal of cadmium from aqueous solution by magnetic biochar: Adsorption characteristics and mechanism. *Environ. Sci. Pollut. Res.* **2024**, *31*, 6543–6557. [CrossRef]
49. Wu, W.L.; Liu, Z.H.; Azeem, M.; Guo, Z.Q.; Li, R.H.; Li, Y.G.; Peng, Y.R.; Ali, E.F.; Wang, H.L.; Wang, S.S.; et al. Hydroxyapatite tailored hierarchical porous biochar composite immobilized Cd(II) and Pb(II) and mitigated their hazardous effects in contaminated water and soil. *J. Hazard. Mater.* **2022**, *437*, 129330. [CrossRef]
50. Li, X.F.; Guo, C.L.; Jin, X.H.; He, C.C.; Dang, Z. Mechanisms of Cr(VI) adsorption on schwertmannite under environmental disturbance: Changes in surface complex structures. *J. Hazard. Mater.* **2021**, *416*, 125781. [CrossRef]
51. Wang, H.Y.; Gao, B.; Wang, S.S.; Fang, J.; Xue, Y.W.; Yang, K. Removal of Pb(II), Cu(II), and Cd(II) from aqueous solutions by biochar derived from $KMnO_4$ treated hickory wood. *Bioresour. Technol.* **2015**, *197*, 356–362. [CrossRef] [PubMed]
52. Yu, W.; Hu, J.; Yu, Y.; Ma, D.; Gong, W.; Qiu, H.; Hu, Z.; Gao, H.W. Facile preparation of sulfonated biochar for highly efficient removal of toxic Pb(II) and Cd(II) from wastewater. *Sci. Total Environ.* **2021**, *750*, 141545. [CrossRef] [PubMed]
53. Cai, T.; Liu, X.; Zhang, J.; Tie, B.; Lei, M.; Wei, X.; Peng, O.; Du, H. Silicate-modified oiltea camellia shell-derived biochar: A novel and cost-effective sorbent for cadmium removal. *J. Clean. Prod.* **2021**, *281*, 125390. [CrossRef]